



Cite this: DOI: 10.1039/d2cp03612f

# Length dependence thermal conductivity of zinc selenide (ZnSe) and zinc telluride (ZnTe) – a combined first principles and frequency domain thermorefectance (FDTR) study

 Rajmohan Muthaiah,<sup>a</sup> Roshan Sameer Annam,<sup>a</sup> Fatema Tarannum,<sup>a</sup> Ashish Kumar Gupta,<sup>b</sup> Jivtesh Garg<sup>a</sup> and Shamsul Arafin<sup>c</sup>

In this study, we report the length dependence of thermal conductivity ( $k$ ) of zinc blende-structured Zinc Selenide (ZnSe) and Zinc Telluride (ZnTe) for length scales between 10 nm and 10  $\mu\text{m}$  using first-principles computations, based on density-functional theory. The  $k$  value of ZnSe is computed to decrease significantly from 22.9  $\text{W m}^{-1} \text{K}^{-1}$  to 1.8  $\text{W m}^{-1} \text{K}^{-1}$  as the length scale is diminished from 10  $\mu\text{m}$  to 10 nm. The  $k$  value of ZnTe is also observed to decrease from 12.6  $\text{W m}^{-1} \text{K}^{-1}$  to 1.2  $\text{W m}^{-1} \text{K}^{-1}$  for the same decrease in length. We also measured the  $k$  of bulk ZnSe and ZnTe using the Frequency Domain Thermorefectance (FDTR) technique and observed a good agreement between the FDTR measurements and first principles calculations for bulk ZnSe and ZnTe. Understanding the thermal conductivity reduction at the nanometer length scale provides an avenue to incorporate nanostructured ZnSe and ZnTe for thermoelectric applications.

 Received 5th August 2022,  
 Accepted 25th October 2022

DOI: 10.1039/d2cp03612f

[rsc.li/pccp](http://rsc.li/pccp)

## Introduction

With the development of improved manufacturing capabilities, the field of microelectronics has advanced significantly,<sup>1–3</sup> leading to a significant reduction in the sizes of the transistors being used, as predicted by Moore's Law.<sup>4</sup> As the length scale of the materials approaches nanometers,<sup>5</sup> the thermal conductivity exhibited by these materials changes significantly,<sup>6–16</sup> where a reduction in size leads to a significant drop in their thermal conductivity,<sup>17</sup> leading to a rise in the working temperature in electronic applications. This phenomenon diminishes the reliability and performance in microelectronics.<sup>18</sup> Hence, effective thermal management has received significant attention as an area of concern in the design of modern microelectronics.<sup>7,9,12,15,19,20</sup> A low thermal conductivity can also be beneficial for applications, such as in thermoelectrics, where the lower lattice thermal conductivity minimizes heat loss through lattice vibrations, improving the energy conversion efficiency. Many techniques such as Scanning Thermal Microscopy (SThM),<sup>21</sup> Time Domain Thermorefectance (TDTR)<sup>22–24</sup> and Frequency Domain

Thermorefectance (FDTR)<sup>25</sup> have been used to understand and gain insight into the transport phenomena at the nanometer length scale.

Zinc chalcogenides (ZnX, X = S, Se and Te) are II–VI wide band gap semiconductors that crystallize with the zinc blende crystal structure,<sup>26–31</sup> and are mainly studied for their catalytic,<sup>32</sup> electronic,<sup>33,34</sup> structural,<sup>34</sup> opto-electronic,<sup>35</sup> thermal<sup>29,36</sup> and thermoelectric properties.<sup>37</sup> In recent times, thin films and nanostructured ZnSe have been widely investigated,<sup>28,37</sup> however, their thermal conductivity dependence on size is unknown. In this work, we report the bulk and length dependent lattice thermal conductivity ( $k$ ) of ZnSe and ZnTe by solving the phonon Boltzmann transport equation (PBTE) coupled with harmonic and anharmonic interatomic force interactions derived from density-functional theory.<sup>38–40</sup> At 300 K, our first-principles estimated  $k$  values of isotopically pure ZnSe and ZnTe to be 25.4  $\text{W m}^{-1} \text{K}^{-1}$  and 15.2  $\text{W m}^{-1} \text{K}^{-1}$ , respectively. The  $k$  values of isotopically disordered ZnSe and ZnTe are 23.2  $\text{W m}^{-1} \text{K}^{-1}$  and 14.2  $\text{W m}^{-1} \text{K}^{-1}$ , respectively. Based on good agreement with previous studies,<sup>41</sup> we computed length dependent  $k$  of ZnSe and ZnTe by including Casimir scattering.<sup>42</sup>

We first discuss the details of our computation of the bulk and length dependent  $k$  of ZnSe and ZnTe using first principles calculations, together with details of the FDTR setup for measurement of the  $k$  values of polycrystalline ZnSe and ZnTe,<sup>25,43–46</sup> followed by the results and discussion. We discuss the phonon dispersions, phonon group

<sup>a</sup> School of Aerospace and Mechanical Engineering, University of Oklahoma, Norman, OK 73019, USA. E-mail: rajumenr@ou.edu

<sup>b</sup> Department of Mechanical and Aerospace Engineering, Oklahoma State University, Stillwater, OK 74078, USA

<sup>c</sup> Department of Electrical and Computer Engineering, Ohio State University, Columbus, OH 43210, USA

velocities, phonon scattering rates, phonon mean free paths and mode dependent contribution of transverse acoustic (TA), longitudinal acoustic (LA) and optical phonons for both ZnSe and ZnTe, as well as the length dependence and mean free path accumulation of  $k$  for the two materials.

We also provide a brief description of FDTR, which is a non-destructive, non-contact<sup>45</sup> method of measuring the thermal properties of a material. This experimental method utilizes an optical pump-probe technique that comprises of a pump laser, which provides a sinusoidal heat signal to the material under study, and a probe laser, which measures the corresponding phase lag of the temperature, relative to the heat signal provided by the pump laser. In FDTR, the pump laser beam is frequency modulated, and the measurement is carried out across a range of frequencies. The frequency of modulation is supplied using a signal generator,<sup>43,46</sup> where, in this case, the lock-in amplifier<sup>43,46</sup> is capable of generating input signals of up to 50 MHz and the frequency range utilized for these measurements was 2 kHz to 50 MHz. The sample is coated with a thin layer ( $\sim 100$  nm) of gold, which has a high coefficient of thermorefectance at the probe beam wavelength (532 nm). Each measurement is performed by fitting the measured phase lag induced by the material,  $\varphi = \varphi_{\text{pump}} - \varphi_{\text{probe}}$ , to the phase lag that is predicted using a 2D heat conduction model, which involves various input parameters such as the transducer thickness, the thermal properties of the thin film metal transducer, and the effective spot size of the probe beam that was measured during the experiment. Various combinations of thermal and geometrical properties can be extracted with great confidence, from this measurement. These measurements are also useful for identifying the isotropy/anisotropy of the materials.<sup>47–50</sup> FDTR is a versatile measurement technique and can be used to measure the thermal properties of a wide range of material systems such as solids,<sup>22,25,46,51,52</sup> liquids,<sup>46,53,54</sup> and thin films,<sup>46,55–57</sup> as well as the thermal conductance of interfaces.<sup>58–61</sup>

## Computational details

The thermal conductivity in this work is computed by solving the phonon Boltzmann transport equation (PBTE) described below,

$$-c(\mathbf{q}s) \cdot \nabla T \left( \frac{\partial n_{\mathbf{q}s}}{\partial T} \right) + \frac{\partial n_{\mathbf{q}s}}{\partial T} \Big|_{\text{scatt}} = 0$$

where  $n_{\mathbf{q}s}$  is the population of the phonon mode with the wave-vector  $\mathbf{q}$  and polarization  $s$ ,  $T$  is the temperature and  $c(\mathbf{q}s)$  is the phonon group velocity computed using  $c(\mathbf{q}s) = \partial \omega_{\mathbf{q}s} / \partial \mathbf{q}$  (where  $\omega_{\mathbf{q}s}$  represents the frequency of the phonon mode  $\mathbf{q}s$ ). The PBTE represents a balance between the change in phonon population due to the temperature gradient (the first term in the equation) and the change in population due to scattering (the second term). In this work, the PBTE is solved exactly for the phonon population using the QUANTUM ESPRESSO thermal2 code. Knowledge of the perturbed phonon populations enables the computation of thermal conductivity.

The only ingredients required to compute all phonon properties involved in the PBTE are the second-order (harmonic) and third-order (anharmonic) interatomic force interactions. These force interactions were derived accurately in this work from first-principles. Harmonic force interactions are needed to compute the phonon frequencies, group velocities and populations, and anharmonic force interactions enable the computation of phonon scattering. The harmonic interactions were derived using the PHONON code,<sup>62</sup> and the anharmonic interactions were derived using the D3Q package,<sup>63,64</sup> both within the QUANTUM ESPRESSO density-functional theory (DFT) code.

All the first principles calculations were performed using the plane-wave based QUANTUM ESPRESSO<sup>65</sup> package. We used the local density approximation (LDA)<sup>66</sup> and norm-conserving pseudopotentials for electronic calculations. Calculations were carried out with a plane-wave energy cut-off of 80 Ry, and a Monkhorst-Pack<sup>67</sup>  $k$ -point mesh of  $12 \times 12 \times 12$  was used for integration over the Brillouin zone. The crystal structure was relaxed until the total force acting on each atom diminished below  $1 \times 10^{-5}$  eV  $\text{\AA}^{-1}$ . The optimized lattice constants of zinc blende crystal-structured ZnSe and ZnTe were determined to be  $a = 5.6$   $\text{\AA}$  and  $a = 6.138$   $\text{\AA}$ , respectively. Dynamical matrices were computed on a  $8 \times 8 \times 8$   $\mathbf{q}$ -grid mesh. An inverse Fourier transform was used to convert these matrices in  $\mathbf{q}$ -space into 2nd order force constants (harmonic) in real space on an  $8 \times 8 \times 8$  supercell. The anharmonic (3rd order) interatomic force constants were similarly first computed on a  $4 \times 4 \times 4$   $\mathbf{q}$ -grid using the QUANTUM ESPRESSO D3Q<sup>62–64</sup> package, and were then inverse-Fourier transformed to obtain the force constants in real space. The lattice thermal conductivity is calculated by solving the Peierls-Boltzmann transport equation (PBTE)<sup>62,64,68</sup> iteratively within the QUANTUM ESPRESSO thermal2 code<sup>62–64</sup> with a  $30 \times 30 \times 30$   $\mathbf{q}$ -mesh. Casimir scattering<sup>42</sup> imposed for the length dependence  $k$  calculations.

## Experimental setup<sup>45,46</sup>

The FDTR system setup (Fig. 1) consists of two 20 mW continuous-wave free space diode lasers (Coherent OBIS), namely, the pump laser (blue), which works at the wavelength of 473 nm, and the probe laser (green), which operates at the wavelength of 532 nm. The pump laser is modulated digitally using the output reference of the lock-in amplifier (Zurich Instruments HF2LI). The driving signal used for pump laser modulation is a sinusoidal signal with a 2 V peak-to-peak voltage and a frequency ranging from 2 kHz to 50 MHz. The beams from these lasers pass through optical isolators (Thorlabs IO-5-532-HP for 532 nm, Thorlabs IO-3-488-HP for 473 nm), which prevent any backscattering of the laser beam into the aperture of the laser, thus protecting the two lasers from output power instabilities. The setup also utilizes mirrors to appropriately direct the laser beam in the desired direction. Using a beam splitter, 1% of the pump laser beam is directed towards a photodetector that records the phase of the pump beam, which is referred to as the pump phase or  $\varphi_{\text{pump}}$ .

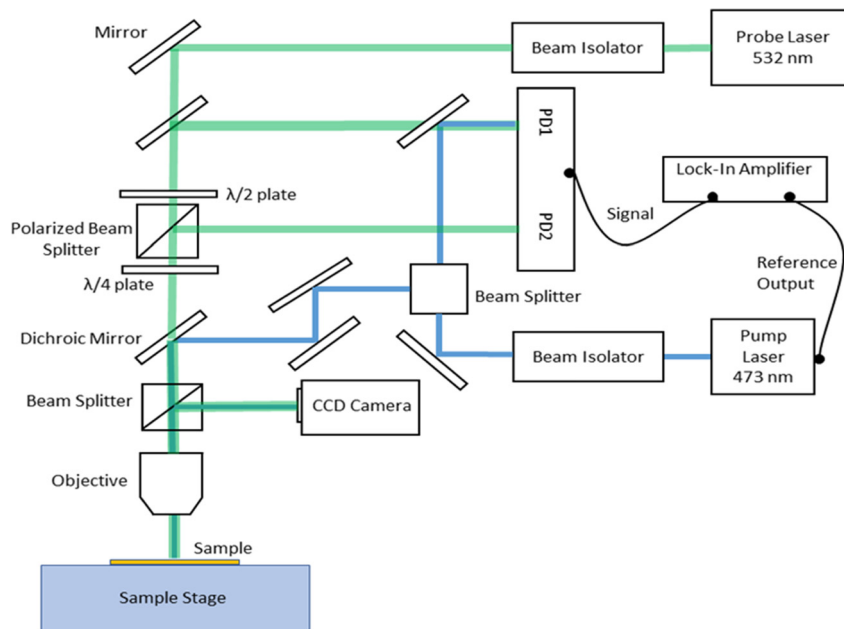


Fig. 1 Frequency domain thermoreflectance (FDTR) experimental setup.

A dichroic mirror (Edmund Optics, hot mirror) reflects the pump beam onto the sample through the microscopic objective. This creates a periodic heat flux on the sample's surface with the spot intensity being at a maximum in the middle and decaying towards the edges, according to a Gaussian spatial distribution. Both the pump and probe beams are aligned coaxially, and the probe beam is used to measure the change in phase of the temperature response of the surface with respect to the phase of the input heat signal. This is achieved by measuring the surface temperature *via* measurement of the intensity of the reflected probe beam (the two are correlated through the fact that the surface reflectivity is a function of the surface temperature). Every sample whose thermal properties are measured using FDTR utilizes a thin film of metal, whose thickness is in the range of 80–100 nm. The metal film maximizes the coefficient of thermo-reflectance at the probe beam's operating wavelength. Balanced photodetection is implemented to improve the signal-to-noise ratios at the low frequencies of modulation for the pump laser. A balanced photodetector such as a Thorlabs PDB415A is used, as it consists of two well matched photodiodes, namely, PD1 and PD 2. A polarizing beam splitter (PBS) is utilized to split the probe beam into a pre-sample beam and a post-sample beam. The pre-sample beam is reflected into PD2 as shown in the schematic (Fig. 1). The post-sample beam is reflected from the sample surface and reflected again using the dichroic mirror into PD1. In order to reduce noise in the PD signal, the optical path lengths to PD1 and PD2 need to be matched. This noise minimization is achieved by delicately balancing the pre- and post-sample beams, by adjusting the half-wave plate. Another means of noise rejection that has been implemented is by letting the subtracted signal of PD1 and PD2 pass through a low noise transimpedance amplifier. This method helps to eliminate noise from the probe beam, which is

a common problem in the measurements. To prevent the thermal signal from being overwhelmed by the backscattering of the pump beam, two band pass filters (FGB37) are used before the photodetectors.

The measurement using FDTR in our case works by comparing the phase lag of the probe beam's post-sample beam (as discussed earlier) with respect to the phase of the periodic pump beam heat source. It is important to note that all the components within the experimental setup along with the path lengths traversed by both the pump and probe beams introduces a frequency-dependent phase shift to the signal which is denoted by  $\varphi_{\text{ext}}$ . This phase shift is accounted for, by sampling 1% of the pump beam and directing it into the post-sample photodetector. Then,  $\varphi_{\text{ext}}$  is measured over a range of modulation frequencies for the pump beam and is subtracted from the phase signal that has been measured, before fitting the measured data to a thermal model. In the setup, we also use a translation stage to adjust the sample height, which keeps the sample in sharp focus, *i.e.*, the sample is in the depth of focus of the objective lens being used. This step is of utmost importance as a sharp image of a focused sample helps in the accurate determination of the spot size, which is a vital input parameter for the thermal model. The image of the sample being focused is obtained using a CCD (charge-coupled device) camera.

The ZnSe and ZnTe bulk crystals were purchased from MTI Corporation. The gold pellet for deposition of the gold<sup>45,48,69</sup> thin film on bulk polycrystalline ZnSe was purchased from the Kurt J. Lesker Company (99% purity). We used a Lesker Nano36 Evaporator thermal evaporator (part of Microfabrication Research & Education Center at the University of Oklahoma) to deposit the 100 nm thick gold film. After this, the sample was placed carefully on a glass slide using double sided carbon tape, making it ready for measurement using FDTR.

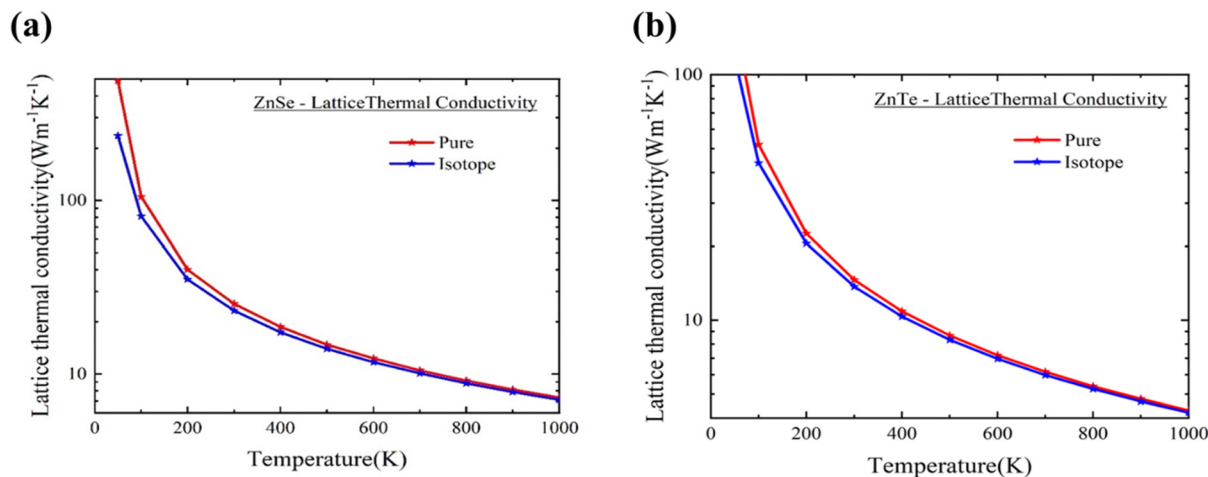


Fig. 2 Lattice thermal conductivity of pure and naturally occurring (a) ZnSe and (b) ZnTe.

## Results and discussions

The temperature dependent lattice thermal conductivity ( $k$ ) of Zinc Selenide (ZnSe) and Zinc Telluride (ZnTe) derived from first-principles computations is shown in Fig. 2(a) and (b), respectively. At room temperature (300 K),  $k = 23.2 \text{ W m}^{-1} \text{ K}^{-1}$  is computed for naturally occurring ZnSe, which is in close agreement with the previously reported experimental value.<sup>29</sup> The length dependent  $k$  of ZnSe nanostructures was computed from first principles calculations, by imposing Casimir/boundary scattering<sup>42</sup> and is shown in Fig. 4(a). Casimir/boundary scattering was imposed by assuming the length to be the same in all three directions, and thus relates to the case of a grain with similar dimensions in all directions. The length-dependent  $k$  value thus computed is isotropic in nature. The  $k$  value of ZnSe is observed to decrease significantly from  $22.9 \text{ W m}^{-1} \text{ K}^{-1}$  to  $1.8 \text{ W m}^{-1} \text{ K}^{-1}$  as the length scale is diminished from  $10 \mu\text{m}$  to  $10 \text{ nm}$  (Fig. 4(a)). The  $k$  of bulk ZnTe is computed to be  $14.17 \text{ W m}^{-1} \text{ K}^{-1}$  for the naturally occurring case, which again is in close agreement with the previously reported values.<sup>41</sup>

The  $k$  value of natural ZnTe is also observed to decrease significantly from  $12.6 \text{ W m}^{-1} \text{ K}^{-1}$  to  $1.2 \text{ W m}^{-1} \text{ K}^{-1}$  as the length scale is diminished from  $10 \mu\text{m}$  to  $10 \text{ nm}$  (Fig. 4(b)). We investigated the phonon dispersion (Fig. 3), phonon group velocity, phonon scattering rate and phonon mean free path in detail to explain these thermal conductivity results.

We first compare the thermal conductivity accumulation (at 300 K) with respect to the phonon mean free path (MFP) in Fig. 5(a) and (b) for ZnSe and ZnTe, respectively.<sup>70</sup> The length dependence of  $k$  (as shown in Fig. 4(a) and (b)) can be understood based on the mean free path accumulation of  $k$ . Fig. 5(a) shows that in ZnSe, phonons with a mean free path below  $100 \text{ nm}$  contribute  $\sim 8 \text{ W m}^{-1} \text{ K}^{-1}$  to the overall  $k$ , which leads to a length dependent  $k$  of  $\sim 8 \text{ W m}^{-1} \text{ K}^{-1}$  at the  $100 \text{ nm}$  length scale for ZnSe. The contributions of transverse acoustic (TA), longitudinal acoustic (LA) and optical phonons to the overall thermal conductivity are shown in Fig. 6(a) and (b) for ZnSe and ZnTe, respectively.

The phonon line widths (*i.e.*, the inverse of the lifetime values) are shown in Fig. 7(a) and (b), and the phonon group velocities are shown in Fig. 8(a) and (b) for ZnSe and ZnTe, respectively.

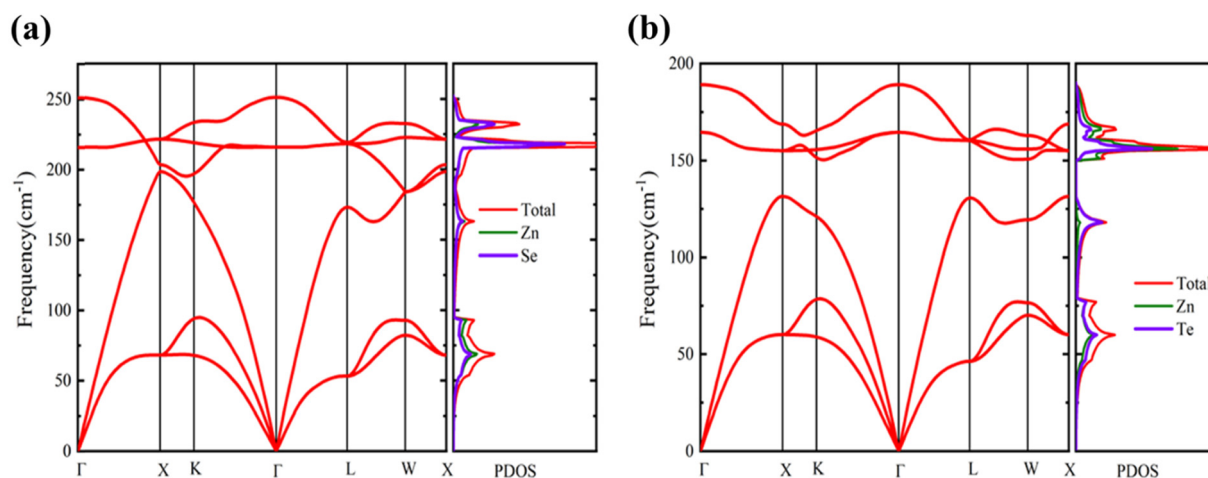


Fig. 3 Phonon dispersion and density of states of (a) ZnSe and (b) ZnTe.

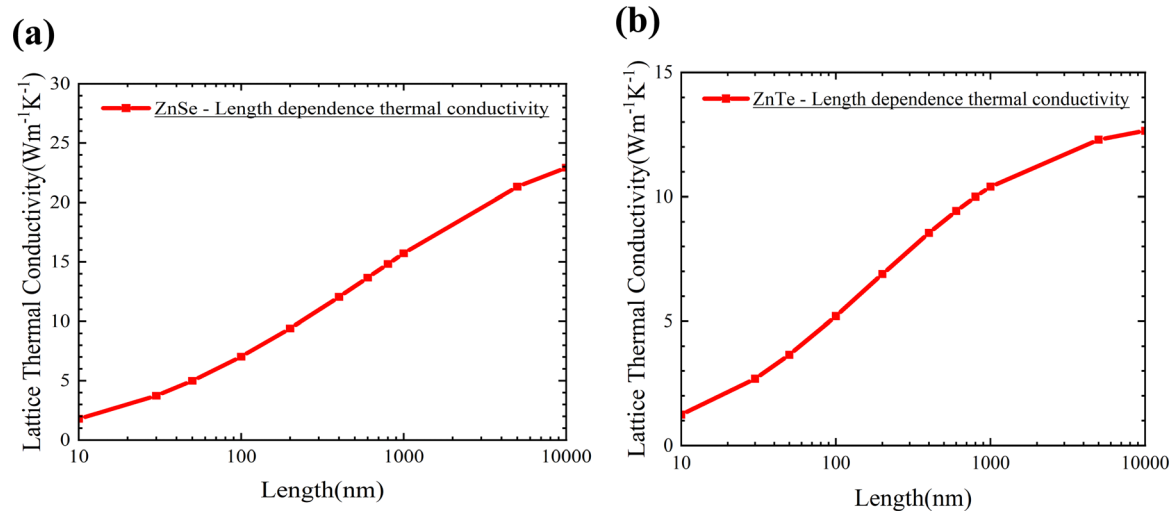


Fig. 4 Length dependent thermal conductivity of isotopically disordered (a) ZnSe and (b) ZnTe.

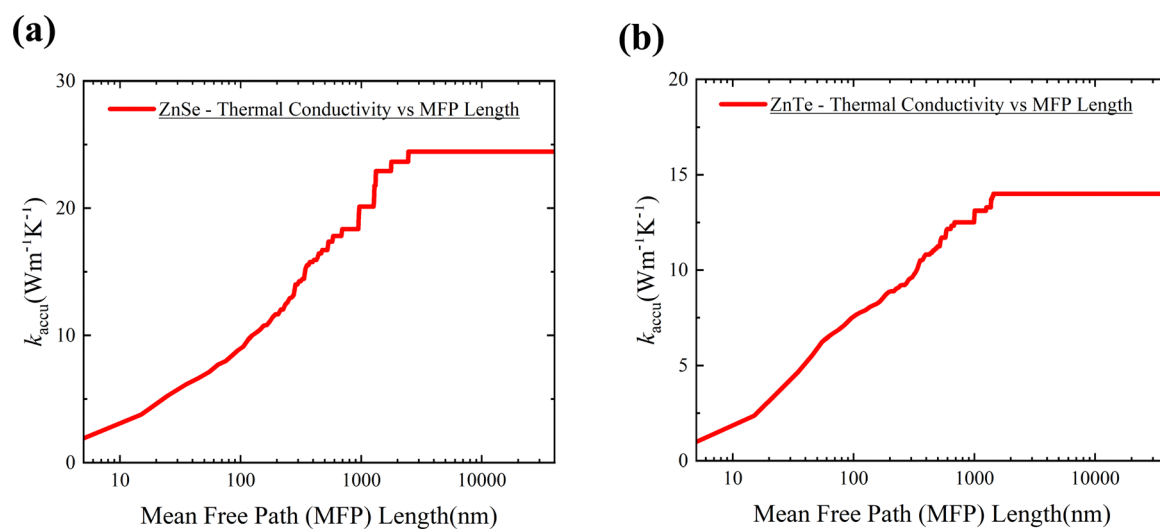


Fig. 5 Mean free path length dependent thermal conductivity of isotopically disordered (a) ZnSe and (b) ZnTe.

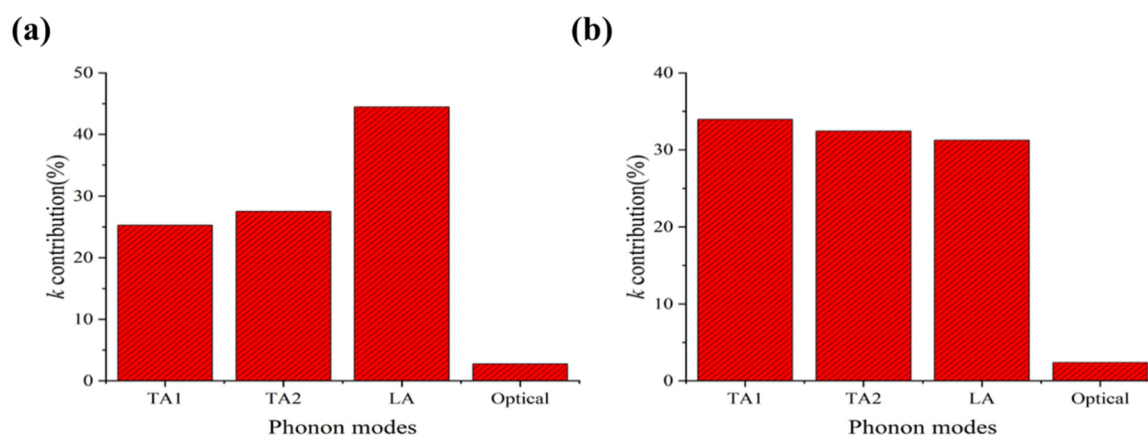


Fig. 6 Thermal conductivity contribution from TA, LA and optical phonon modes for (a) ZnSe and (b) ZnTe.

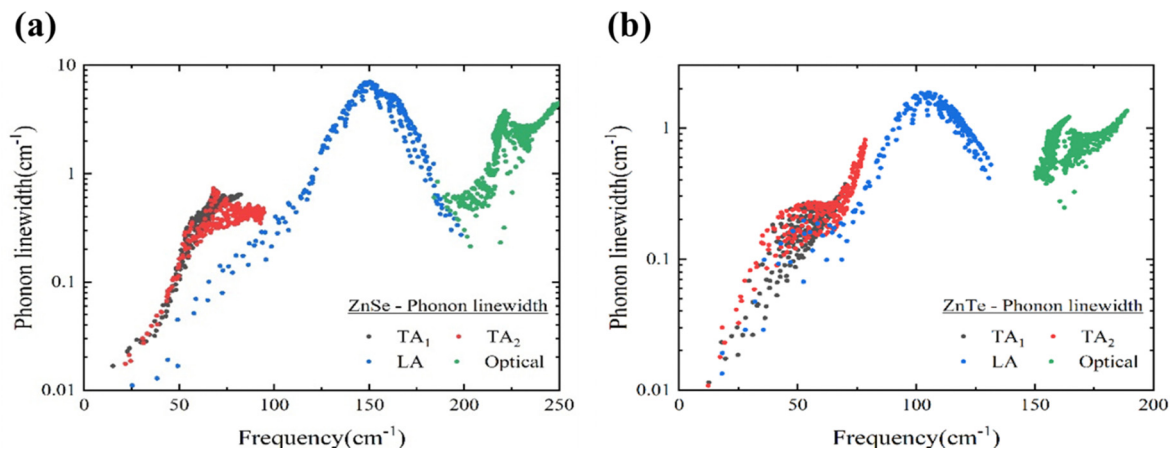


Fig. 7 Phonon scattering rates of (a) ZnSe and (b) ZnTe.

In ZnSe, the contribution of LA phonons to the overall thermal conductivity is higher than TA and optical phonons (Fig. 6(a) and 9). This can be understood by noticing that LA phonons have

higher phonon group velocities (Fig. 8(a)), and their scattering rates (Fig. 7(a)) are lower than TA phonons (in the low frequency range) in ZnSe.

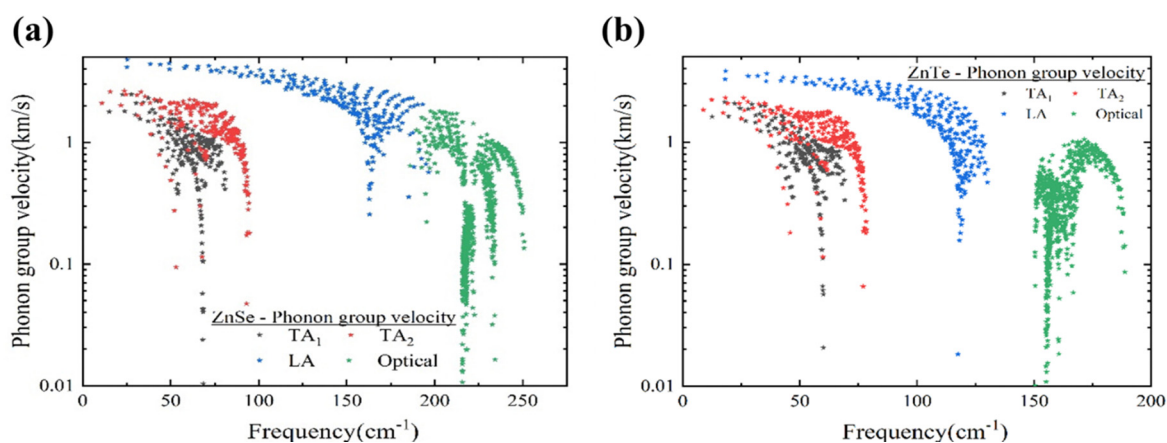


Fig. 8 Phonon group velocities of (a) ZnSe and (b) ZnTe.

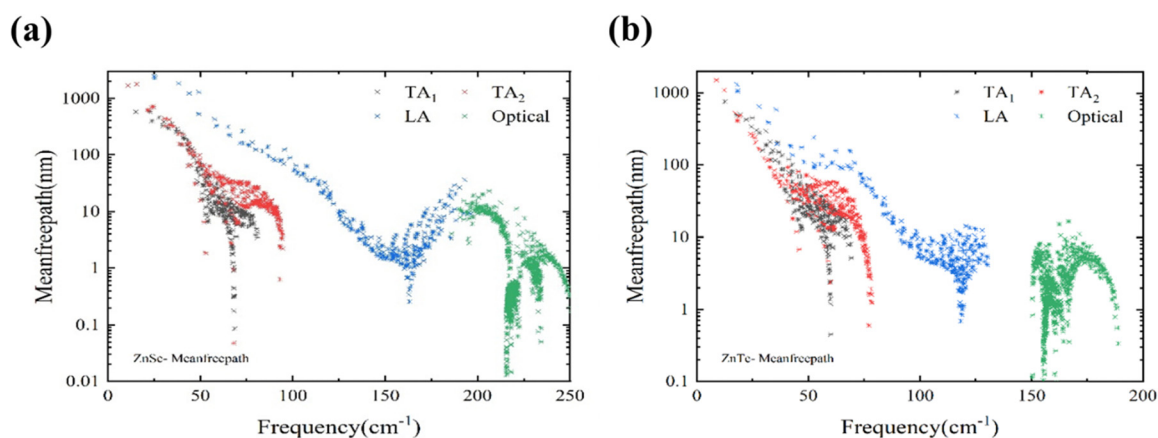


Fig. 9 Phonon mean free paths of (a) ZnSe and (b) ZnTe.

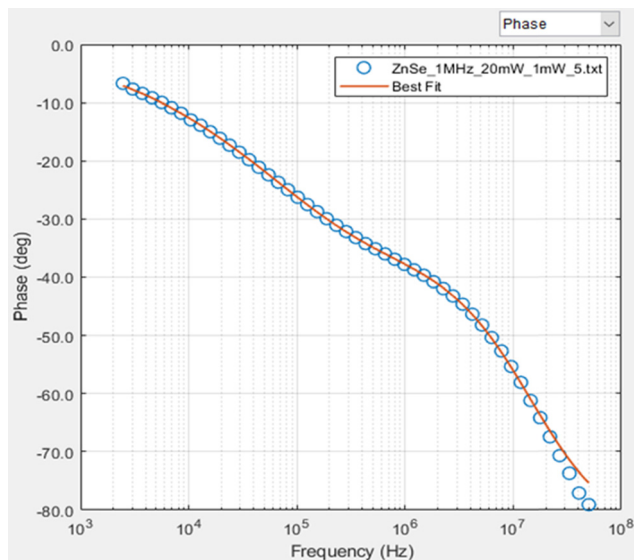


Fig. 10 FDTR data for curve fitting analysis to calculate the thermal properties of ZnSe measured at a lock-in frequency of 1 MHz along with pump and probe powers at 20 and 5 mW, respectively.

LA phonons contribute almost 44.5% to the overall thermal conductivity in ZnSe. In the case of ZnTe, the contribution of  $TA_1$ ,  $TA_2$  and LA phonons is  $\sim 34\%$ ,  $32\%$  and  $31\%$ , respectively, at 300 K.

## FDTR measurements

The experimentally measured thermal conductivity values of Zinc Selenide (ZnSe) and Zinc Telluride (ZnTe) using FDTR were found to be  $\sim 17 \text{ W m}^{-1} \text{ K}^{-1}$  and  $14 \text{ W m}^{-1} \text{ K}^{-1}$ , respectively, at room temperature. By comparing the experimental thermal conductivity results from FDTR with the theoretical results as shown in Fig. 4(a) and (b), we can determine that the grain sizes of the ZnSe and ZnTe samples (obtained from MTI Corp.) are in the range of  $2 \mu\text{m}$  to  $10 \mu\text{m}$ .<sup>71</sup> Measurement of the thermal conductivities of polycrystalline ZnSe and ZnTe using FDTR is achieved using a curve fitting method, as explained in the experimental setup. The blue circles (in Fig. 10) represent the phase-lag data that was measured using the FDTR. The frequency of the lock-in amplifier was set at 1 MHz and the laser power of the pump and probe lasers were set at 20 mW and 5 mW, respectively, for all samples measured in this work. The solid line represents the best fit curve, which is obtained using a 2D heat conduction mathematical model that utilizes known input parameters such as the volumetric heat capacity of the gold film, the gold film thermal conductivity, the film thickness, the volumetric heat capacity of the material under investigation, the thickness of the material under investigation and the laser spot size. The properties of the gold film and its thickness are determined by depositing the gold film over a substrate with known properties, namely, fused silica ( $k \approx 1 \text{ W m}^{-1} \text{ K}^{-1}$ ) and sapphire ( $k \approx 35 \text{ W m}^{-1} \text{ K}^{-1}$ ).

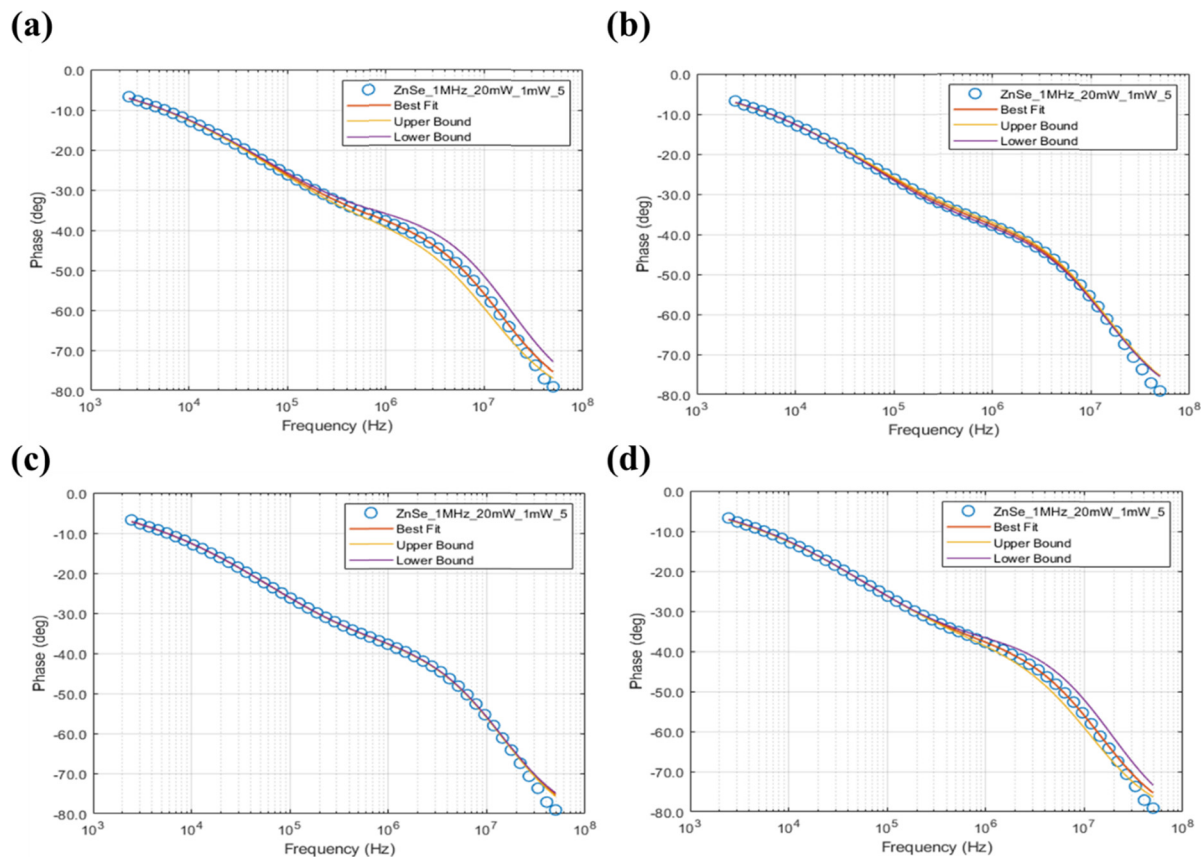


Fig. 11 Sensitivity of phase-lag to the (a) gold volumetric heat capacity, (b) gold cross-plane thermal conductivity, (c) gold in-plane thermal conductivity and (d) thickness of the gold film deposited on top of the ZnSe crystal.

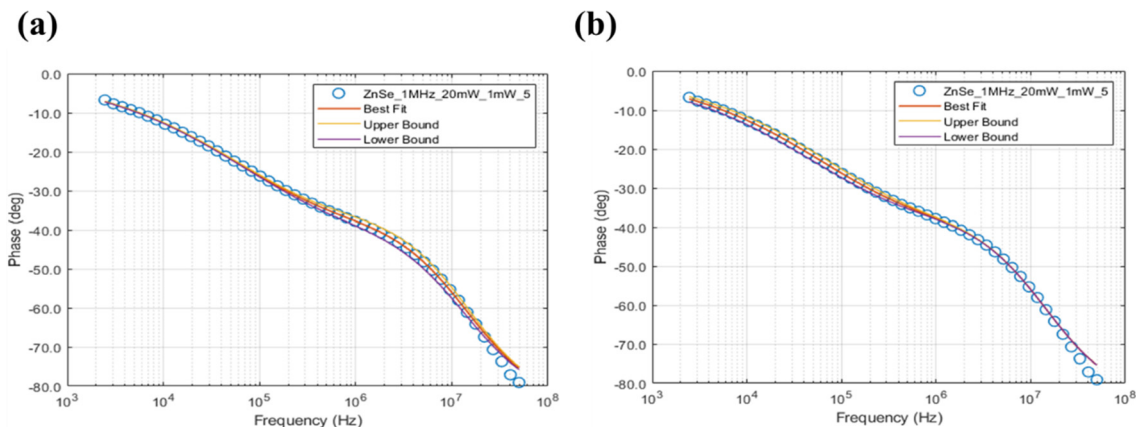


Fig. 12 Sensitivity of the (a) cross-plane and (b) in-plane thermal conductivity parameters of the ZnSe crystal.

This results in the accurate determination of the properties of the gold thin film. The volumetric heat capacities of ZnSe and ZnTe are obtained by multiplying the density ( $\text{g cm}^{-3}$ ) and their specific heat capacity ( $\text{J kg}^{-1} \text{K}^{-1}$ ). These details are available on the datasheets for ZnSe and ZnTe on the MTI Corporation's website.<sup>72</sup> The only unknown property in our study is the thermal conductivity of ZnSe and ZnTe, which leads to a single parameter fit.

For the measured thermal conductivity to be accurate, the measured data and the predicted phase-lag from the heat conduction model should agree very well. As shown in Fig. 10, the best fit curve agrees very well with the measured phase-lag values (represented by blue circles). This figure is representative of the agreement between the measured phase data and the phase data generated using the mathematical model that utilizes the input parameters mentioned earlier in the section.

We next describe the sensitivity analysis, which is important in ascertaining the accuracy of the measured thermal conductivity values. Insensitive parameters can be fixed as input parameters in the model as they do not affect the curve fitting, and this reduces the number of free parameters to be fitted. Sensitive parameters are seen to make a significant difference

in the upper and lower bound values of the phase lag measured in degrees (Fig. 11(a) and (d)), while insensitive parameters demonstrate a small difference between these bounds (Fig. 11(b) and (c)). Fig. 11(a), (b) and (d) show that the measurement is sensitive to the gold thin film's volumetric heat capacity, its cross-plane thermal conductivity and its thickness (essential input parameters). Fig. 12(a) and (b) show that the measurement is sensitive to the cross- and in-plane thermal conductivity of bulk polycrystalline ZnSe. Fig. 13(a) and (b) represent another way of understanding sensitivity in terms of the phase difference values.

As seen in Fig. 13, the sensitivity analysis shown in Fig. 11 and 12 can be represented as a function of the phase lag set to a certain upper and lower bound limit, which in this case is set to 20%. This representation is a great way of determining the sensitivity of FDTR to the material parameters. Comparing Fig. 11(b) and (c) with Fig. 13(a), the orange and yellow curves represent the sensitivity of FDTR to the in-plane and cross-plane thermal conductivities of the gold thin film.

The green and light blue curves in Fig. 13(a) corresponds to the sensitivity of FDTR to the in-plane and cross-plane thermal conductivities of ZnSe.

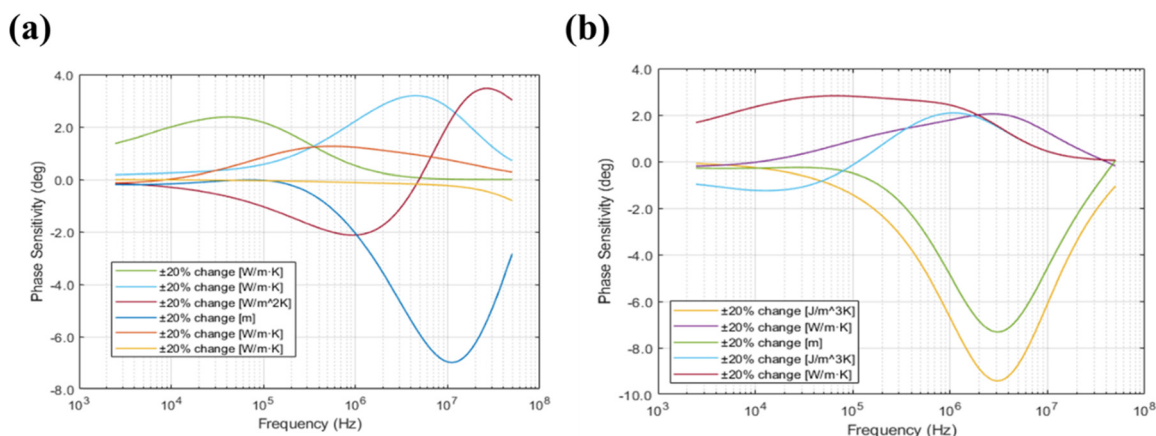


Fig. 13 Sensitivity analysis of all the parameters of the gold transducer and (a) ZnSe and (b) ZnTe as a function of the phase change with limits of  $\pm 20\%$  for the upper and lower bounds.

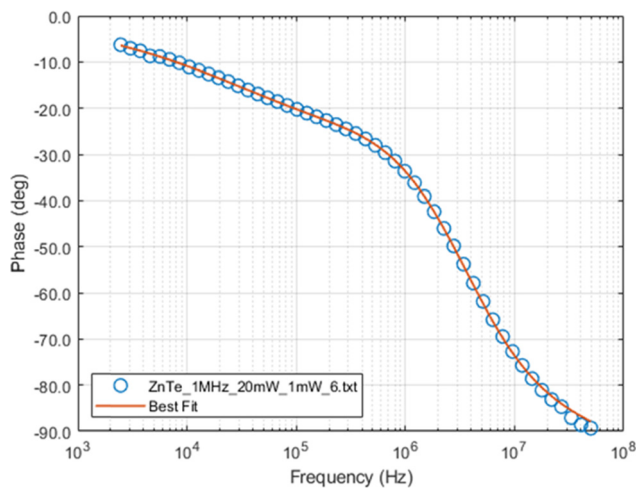


Fig. 14 FDTR data for curve fitting analysis to calculate the thermal properties for ZnTe.

Another analysis process similar to that of ZnSe was conducted for ZnTe, in order to determine its thermal conductivity. Fig. 14 shows that with the help of accurately determined input parameters, we were able to achieve a good agreement between the FDTR measurement of the phase lag and the phase lag calculated using the 2D diffusion model, keeping the thermal conductivity of ZnTe as a floating or a free parameter. This gives us a high confidence value of the thermal conductivity of ZnTe, which was measured to be  $\sim 14 \text{ W m}^{-1} \text{ K}^{-1}$ .

## Conclusion

Using FDTR, the experimentally determined thermal conductivity values of naturally occurring ZnSe and ZnTe were found to be  $\sim 17 \text{ W m}^{-1} \text{ K}^{-1}$  and  $14 \text{ W m}^{-1} \text{ K}^{-1}$ , respectively. These compare well to the computed results of around  $23.2 \text{ W m}^{-1} \text{ K}^{-1}$  and  $14.2 \text{ W m}^{-1} \text{ K}^{-1}$  for naturally occurring ZnSe and ZnTe, respectively, at 300 K achieved using first-principles. The length dependent  $k$  value of ZnSe saw a significant reduction from  $22.9 \text{ W m}^{-1} \text{ K}^{-1}$  to  $1.8 \text{ W m}^{-1} \text{ K}^{-1}$  with the length scale diminishing from  $10 \mu\text{m}$  to  $10 \text{ nm}$ . Similarly, for ZnTe, the  $k$  value was observed to decrease significantly from  $12.6 \text{ W m}^{-1} \text{ K}^{-1}$  to  $1.2 \text{ W m}^{-1} \text{ K}^{-1}$  with a similar length scale reduction as ZnSe. The difference in the experimental and the computational results can be attributed to the dissimilarity in the polycrystallinity as obtained from the manufacturer and as modeled for computational analysis. FDTR can be utilized to measure the thermal properties of unknown material systems with great confidence, and supplemented by computational work, it can enable a greater understanding of the physics of heat transport phenomena within material systems. In addition, this combination of computational and experimental work using FDTR can enable the tuning of materials to achieve the desired results for specific applications in the areas of thermal management and thermoelectric devices.

## Conflicts of interest

There are no conflicts of interest to declare.

## Acknowledgements

RM, RSA, FT and JG acknowledge support from the National Science Foundation award under award no. #2115067. We also acknowledge the OU Supercomputing Center for Education and Research (OSCR) for providing the computing resources for this work.

## References

- 1 G. Teepe The growing importance of microelectronics from a foundry perspective. in 2014 Design, Automation & Test in Europe Conference & Exhibition (DATE). 2014. IEEE.
- 2 A. J. Austin, *et al.*, High-temperature atomic layer deposition of GaN on 1D nanostructures, *Nanomaterial*, 2020, **10**(12), 2434.
- 3 J. Qu, 8.06 – *Thermomechanical Reliability of Microelectronic Packaging*, in *Comprehensive Structural Integrity*, ed. I. Milne, R. O. Ritchie, and B. Karihaloo, Pergamon, Oxford, 2003, pp. 219–239.
- 4 G. E. Moore, Cramming more components onto integrated circuits, *Proc. IEEE*, 1998, **86**(1), 82–85.
- 5 S. Mandal, *et al.*, Atomic-scale insights on large-misfit heterointerfaces in LSMO/MgO/c-Al<sub>2</sub>O<sub>3</sub>, *Crystals*, 2021, **11**(12), 1493.
- 6 R. Muthaiah, *et al.*, First principles investigation of high thermal conductivity in hexagonal boron phosphide, *arXiv*, 2022, preprint, arXiv:2201.09430, DOI: [10.48550/arXiv.2201.09430](https://doi.org/10.48550/arXiv.2201.09430).
- 7 R. Muthaiah, J. Garg and S. Arafin, Ultrahard BC5 – An efficient nanoscale heat conductor through dominant contribution of optical phonons, *Comput. Mater. Sci.*, 2022, **206**, 111276.
- 8 R. Muthaiah, F. Tarannum and J. Garg, Strain tuned low thermal conductivity in indium antimonide (InSb) through increase in anharmonic phonon scattering-A first-principles study, *Solid State Commun.*, 2021, **334**, 114378.
- 9 R. Muthaiah and J. Garg, First principles investigation of high thermal conductivity in hexagonal germanium carbide(2H-GeC), *Carbon Trends*, 2021, **5**, 100113.
- 10 R. Muthaiah and J. Garg, Thermal conductivity of magnesium telluride (MgTe)-A first principles study, *Solid State Commun.*, 2021, **337**, 114414.
- 11 R. Muthaiah and J. Garg, Thermal conductivity of magnesium selenide (MgSe)-A first principles study, *Comput. Mater. Sci.*, 2021, **198**, 110679.
- 12 R. Muthaiah and J. Garg, Ultrahigh thermal conductivity in hexagonal BC6N-An efficient material for nanoscale thermal management-A first principles study, *Comput. Mater. Sci.*, 2021, **200**, 110773.
- 13 R. Muthaiah and J. Garg, Strain tuned thermal conductivity reduction in indium arsenide (InAs)-A first-principles study, *Comput. Mater. Sci.*, 2021, **196**, 110531.

- 14 R. Muthaiah, *Thermal transport in polymers, polymer nanocomposites and semiconductors using molecular dynamics simulation and first principles study*, PhD thesis, University of Oklahoma, 2021.
- 15 R. Muthaiah, *et al.*, Thermal conductivity of hexagonal BC2P – a first-principles study, *RSC Adv.*, 2020, **10**(70), 42628–42632.
- 16 R. Muthaiah and J. Garg, Strain tuned high thermal conductivity in boron phosphide at nanometer length scales – a first-principles study, *Phys. Chem. Chem. Phys.*, 2020, 20914–20921.
- 17 L. Yang, N. Yang and B. Li, Reduction of thermal conductivity by nanoscale 3D phononic crystal, *Sci. Rep.*, 2013, **3**(1), 1–5.
- 18 J. Due and A. J. Robinson, Reliability of thermal interface materials: A review, *Appl. Therm. Eng.*, 2013, **50**(1), 455–463.
- 19 Z. Tian, *et al.*, On the importance of optical phonons to thermal conductivity in nanostructures, *Appl. Phys. Lett.*, 2011, **99**(5), 053122.
- 20 R. Muthaiah and J. Garg, Strain tuned high thermal conductivity in boron phosphide at nanometer length scales – a first-principles study, *Phys. Chem. Chem. Phys.*, 2020, **22**(36), 20914–20921.
- 21 O. Kwon, L. Shi and A. Majumdar, Scanning thermal wave microscopy (STWM), *J. Heat Transfer*, 2003, **125**(1), 156–163.
- 22 C. A. Paddock and G. L. Eesley, Transient thermoreflectance from thin metal films, *J. Appl. Phys.*, 1986, **60**(1), 285–290.
- 23 W. S. Capinski and H. J. Maris, Improved apparatus for picosecond pump-and-probe optical measurements, *Rev. Sci. Instrum.*, 1996, **67**(8), 2720–2726.
- 24 D. G. Cahill, Analysis of heat flow in layered structures for time-domain thermoreflectance, *Rev. Sci. Instrum.*, 2004, **75**(12), 5119–5122.
- 25 A. J. Schmidt, R. Cheaito and M. Chiesa, A frequency-domain thermoreflectance method for the characterization of thermal properties, *Rev. Sci. Instrum.*, 2009, **80**(9), 094901.
- 26 J. Ding, *et al.*, Thermoelectric transport properties in chalcogenides ZnX (X = S, Se): From the role of electron-phonon couplings, *J. Mater. Chem.*, 2021, **7**(2), 310–319.
- 27 H. Zhang and Y. Fang, Temperature dependent photoluminescence of surfactant assisted electrochemically synthesized ZnSe nanostructures, *J. Alloys Compd.*, 2019, **781**, 201–208.
- 28 T. M. Khan, *et al.*, Synthesis of thermally evaporated ZnSe thin film at room temperature, *Thin Solid Films*, 2011, **519**(18), 5971–5977.
- 29 N. V. Lugueva, S. M. Luguev and A. A. Dunaev, Thermal conductivity of polycrystalline zinc selenide, *Phys. Solid State*, 2003, **45**(3), 449–452.
- 30 R. Chandramohan, C. Sanjeeviraja and T. Mahalingam, Preparation of zinc selenide thin films by electrodeposition technique for solar cell applications, *Phys. Status Solidi A*, 1997, **163**(2), 11–12.
- 31 H. Morkoç, *et al.*, Large-band-gap SiC, III–V nitride, and II–VI ZnSe-based semiconductor device technologies, *J. Appl. Phys.*, 1994, **76**(3), 1363–1398.
- 32 P. Li and T. He, Recent advances in zinc chalcogenide-based nanocatalysts for photocatalytic reduction of CO<sub>2</sub>, *J. Mater. Chem. A*, 2021, **9**(41), 23364–23381.
- 33 D. W. Langer and C. J. Vesely, Electronic core levels of zinc chalcogenides, *Phys. Rev. B: Solid State*, 1970, **2**(12), 4885–4892.
- 34 R. Gangadharan, *et al.*, Electronic and structural properties of zinc chalcogenides ZnX (X = S, Se, Te), *J. Alloys Compd.*, 2003, **359**(1–2), 22–26.
- 35 Y. Sun, *et al.*, Fabrication of flexible and freestanding zinc chalcogenide single layers, *Nat. Commun.*, 2012, **3**(1), 1057.
- 36 K. Davami, *et al.*, Thermal conductivity of ZnTe nanowires, *J. Appl. Phys.*, 2013, **114**(13), 134314.
- 37 Y. Sun, *et al.*, Fabrication of flexible and freestanding zinc chalcogenide single layers, *Nat. Commun.*, 2012, **3**(1), 1–7.
- 38 D. Broido, L. Lindsay and T. Reinecke, *Ab initio* study of the unusual thermal transport properties of boron arsenide and related materials, *Phys. Rev. B: Condens. Matter Mater. Phys.*, 2013, **88**(21), 214303.
- 39 D. A. Broido, *et al.*, Intrinsic lattice thermal conductivity of semiconductors from first principles, *Appl. Phys. Lett.*, 2007, **91**(23), 231922.
- 40 J. Garg, *et al.*, Role of disorder and anharmonicity in the thermal conductivity of silicon-germanium alloys: A first-principles study, *Phys. Rev. Lett.*, 2011, **106**(4), 045901.
- 41 W. M. Haynes, *CRC Handbook of Chemistry and Physics*, CRC Press, 2011.
- 42 H. B. G. Casimir, Note on the conduction of heat in crystals, *Physica*, 1938, **5**(6), 495–500.
- 43 K. Regner, S. Majumdar and J. A. Malen, Instrumentation of broadband frequency domain thermoreflectance for measuring thermal conductivity accumulation functions, *Rev. Sci. Instrum.*, 2013, **84**(6), 064901.
- 44 J. Zhu, *et al.*, Ultrafast thermoreflectance techniques for measuring thermal conductivity and interface thermal conductance of thin films, *J. Appl. Phys.*, 2010, **108**(9), 094315.
- 45 J. Yang, C. Maragliano and A. J. Schmidt, Thermal property microscopy with frequency domain thermoreflectance, *Rev. Sci. Instrum.*, 2013, **84**(10), 104904.
- 46 J. Yang, *Thermal property measurement with frequency domain thermoreflectance*, Boston University, 2016.
- 47 X. Qian, *et al.*, Accurate measurement of in-plane thermal conductivity of layered materials without metal film transducer using frequency domain thermoreflectance, *Rev. Sci. Instrum.*, 2020, **91**(6), 064903.
- 48 P. Jiang, X. Qian and R. Yang, A new elliptical-beam method based on time-domain thermoreflectance (TDTR) to measure the in-plane anisotropic thermal conductivity and its comparison with the beam-offset method, *Rev. Sci. Instrum.*, 2018, **89**(9), 094902.
- 49 J. P. Feser, J. Liu and D. G. Cahill, Pump-probe measurements of the thermal conductivity tensor for materials lacking in-plane symmetry, *Rev. Sci. Instrum.*, 2014, **85**(10), 104903.
- 50 M. Li, J. S. Kang and Y. Hu, Anisotropic thermal conductivity measurement using a new asymmetric-beam time-domain thermoreflectance (AB-TDTR) method, *Rev. Sci. Instrum.*, 2018, **89**(8), 084901.

- 51 J. Liu, *et al.*, Simultaneous measurement of thermal conductivity and heat capacity of bulk and thin film materials using frequency-dependent transient thermoreflectance method, *Rev. Sci. Instrum.*, 2013, **84**(3), 034902.
- 52 C. Wei, *et al.*, Invited article: Micron resolution spatially resolved measurement of heat capacity using dual-frequency time-domain thermoreflectance, *Rev. Sci. Instrum.*, 2013, **84**(7), 071301.
- 53 O. M. Wilson, *et al.*, Colloidal metal particles as probes of nanoscale thermal transport in fluids, *Phys. Rev. B: Condens. Matter Mater. Phys.*, 2002, **66**(22), 224301.
- 54 A. Schmidt, *et al.*, An optical pump-probe technique for measuring the thermal conductivity of liquids, *Rev. Sci. Instrum.*, 2008, **79**(6), 064902.
- 55 A. J. Schmidt, R. Cheaito and M. Chiesa, Characterization of thin metal films *via* frequency-domain thermoreflectance, *J. Appl. Phys.*, 2010, **107**(2), 024908.
- 56 R. M. Costescu, M. A. Wall and D. G. Cahill, Thermal conductance of epitaxial interfaces, *Phys. Rev. B: Condens. Matter Mater. Phys.*, 2003, **67**(5), 054302.
- 57 M. N. Luckyanova, *et al.*, Coherent phonon heat conduction in superlattices, *Science*, 2012, **338**(6109), 936–939.
- 58 H.-K. Lyeo and D. G. Cahill, Thermal conductance of interfaces between highly dissimilar materials, *Phys. Rev. B: Condens. Matter Mater. Phys.*, 2006, **73**(14), 144301.
- 59 P. E. Hopkins, *et al.*, Manipulating thermal conductance at metal-graphene contacts *via* chemical functionalization, *Nano Lett.*, 2012, **12**(2), 590–595.
- 60 P. E. Hopkins, *et al.* Effects of surface roughness and oxide layer on the thermal boundary conductance at aluminum/silicon interfaces. in International Heat Transfer Conference. 2010.
- 61 J. Yang, *et al.*, Thermal conductance imaging of graphene contacts, *J. Appl. Phys.*, 2014, **116**(2), 023515.
- 62 L. Paulatto, *et al.*, First-principles calculations of phonon frequencies, lifetimes, and spectral functions from weak to strong anharmonicity: The example of palladium hydrides, *Phys. Rev. B: Condens. Matter Mater. Phys.*, 2015, **91**(5), 054304.
- 63 L. Paulatto, F. Mauri and M. Lazzeri, Anharmonic properties from a generalized third-order *ab initio* approach: Theory and applications to graphite and graphene, *Phys. Rev. B: Condens. Matter Mater. Phys.*, 2013, **87**(21), 214303.
- 64 G. Fugallo, *et al.*, *Ab initio* variational approach for evaluating lattice thermal conductivity, *Phys. Rev. B: Condens. Matter Mater. Phys.*, 2013, **88**(4), 045430.
- 65 P. Giannozzi, *et al.*, QUANTUM ESPRESSO: A modular and open-source software project for quantum simulations of materials, *J. Phys.: Condens. Matter*, 2009, **21**(39), 395502.
- 66 D. M. Ceperley and B. J. Alder, Ground state of the electron gas by a stochastic method, *Phys. Rev. Lett.*, 1980, **45**(7), 566–569.
- 67 H. J. Monkhorst and J. D. Pack, Special points for Brillouin-zone integrations, *Phys. Rev. B: Solid State*, 1976, **13**(12), 5188–5192.
- 68 J. Garg, N. Bonini and N. Marzari, *First-principles determination of phonon lifetimes, mean free paths, and thermal conductivities in crystalline materials: pure silicon and germanium, in length-scale dependent phonon interactions*, ed. S. L. Shindé and G. P. Srivastava, 2014, Springer, New York, New York, NY, pp. 115–136.
- 69 P. Jiang, X. Qian and R. Yang, Tutorial: Time-domain thermoreflectance (TDTR) for thermal property characterization of bulk and thin film materials, *J. Appl. Phys.*, 2018, **124**(16), 161103.
- 70 Q. Hao, Y. Xiao and Q. Chen, Determining phonon mean free path spectrum by ballistic phonon resistance within a nanoslot-patterned thin film, *Mater. Today Phys.*, 2019, **10**, 100126.
- 71 Q. Hao and J. Garg, A review on phonon transport within polycrystalline materials, *ES Mater. Manuf.*, 2021, **14**, 36–50.
- 72 <https://www.mtixtl.com/crystalssubstratesa-z.aspx>.